

# Spin-excitation anisotropy in the nematic state of detwinned FeSe

Xingye Lu (✉ [luxy@bnu.edu.cn](mailto:luxy@bnu.edu.cn))

Beijing Normal University <https://orcid.org/0000-0002-0409-1240>

Wenliang Zhang

Paul Scherrer Institute

Yi Tseng

Paul Scherrer Institute

Ruixian Liu

Beijing Normal University

Zhen Tao

Beijing Normal University

Eugenio Paris

Paul Scherrer Institute <https://orcid.org/0000-0002-3418-8828>

Panpan Liu

Beijing Normal University

Tong Chen

Rice University

Yu Song

Zhejiang University

Rong Yu

Renmin University of China <https://orcid.org/0000-0001-5936-1159>

Qimiao Si

Rice University <https://orcid.org/0000-0003-1357-2705>

Pengcheng Dai

Rice University

Thorsten Schmitt

Paul Scherrer Institut <https://orcid.org/0000-0002-5737-1094>

---

## Article

**Keywords:** spin-excitation anisotropy, detwinned FeSe, nematic phase transition

**Posted Date:** August 19th, 2021

DOI: <https://doi.org/10.21203/rs.3.rs-774408/v1>

**License:**  This work is licensed under a Creative Commons Attribution 4.0 International License.

[Read Full License](#)

---

1      **Spin-excitation anisotropy in the nematic state of detwinned FeSe**

2      Xingye Lu,<sup>1,\*</sup> Wenliang Zhang,<sup>2</sup> Yi Tseng,<sup>2</sup> Ruixian Liu,<sup>1</sup> Zhen Tao,<sup>1</sup> Eugenio Paris,<sup>2</sup> Panpan Liu,<sup>1</sup>  
3      Tong Chen,<sup>3</sup> Yu Song,<sup>4</sup> Rong Yu,<sup>5</sup> Qimiao Si,<sup>3</sup> Pengcheng Dai,<sup>3,†</sup> and Thorsten Schmitt<sup>2,‡</sup>

4      <sup>1</sup>*Center for Advanced Quantum Studies and Department of Physics,  
5      Beijing Normal University, Beijing 100875, China*

6      <sup>2</sup>*Photon Science Division, Swiss Light Source,  
7      Paul Scherrer Institut, CH-5232 Villigen PSI, Switzerland*

8      <sup>3</sup>*Department of Physics and Astronomy, Rice Center for  
9      Quantum Materials, Rice University, Houston, TX 77005, USA*

10     <sup>4</sup>*Department of Physics, University of California, Berkeley, California 94720, USA*

11     <sup>5</sup>*Department of Physics, Renmin University of China, Beijing 100872, China*

12     (Dated: August 2, 2021)

The origin of the electronic nematicity in FeSe, which occurs below a tetragonal-to-orthorhombic structural transition temperature  $T_s \approx 90$  K, well above the superconducting transition temperature  $T_c = 9$  K, is one of the most important unresolved puzzles in the study of iron-based superconductors. In both spin- and orbital-nematic models, the intrinsic magnetic excitations at  $\mathbf{Q}_1 = (1, 0)$  and  $\mathbf{Q}_2 = (0, 1)$  of twin-free FeSe are expected to behave differently below  $T_s$ . Although anisotropic spin fluctuations below 10 meV between  $\mathbf{Q}_1$  and  $\mathbf{Q}_2$  have been unambiguously observed by inelastic neutron scattering around  $T_c (<< T_s)$ , it remains unclear whether such an anisotropy also persists at higher energies and associates with the nematic transition  $T_s$ . Here we use resonant inelastic x-ray scattering (RIXS) to probe the high-energy magnetic excitations of uniaxial-strain detwinned FeSe. A prominent anisotropy between the magnetic excitations along the  $H$  and  $K$  directions is found to persist to  $\sim 200$  meV, which is even more pronounced than the anisotropy of spin waves in BaFe<sub>2</sub>As<sub>2</sub>. This anisotropy decreases gradually with increasing temperature and finally vanishes at a temperature around the nematic transition temperature  $T_s$ . Our results reveal an unprecedented strong spin-excitation anisotropy with a large energy scale well above the  $d_{xz}/d_{yz}$  orbital splitting, suggesting that the nematic phase transition is primarily spin-driven. Moreover, the measured high-energy spin excitations are dispersive and underdamped, which can be understood from a local-moment perspective. Our findings provide the much-needed understanding of the mechanism for the nematicity of FeSe and points to a unified description of the correlation physics across seemingly distinct classes of Fe-based superconductors.

13     Intertwined order and fluctuations in high transition-temperature ( $T_c$ ) superconductors are pivotal for  
14     understanding the microscopic origin of superconducting electron pairing [1]. Of particular interest is the  
15     electronic nematic state present in both cuprate and iron-based superconductors (FeSCs). Initially discov-

ered through in-plane electronic anisotropy with  $C_2$  symmetry in the paramagnetic orthorhombic state of detwinned  $\text{Ba}(\text{Fe}_{1-x}\text{Co}_x)_2\text{As}_2$  [2–4], the electronic nematic state and its fluctuations have been identified as a ubiquitous feature of FeSC and are believed to be essential to the structural and magnetic transitions in FeSC [5–9], and may enhance the electron pairing for high- $T_c$  superconductivity [10, 11].

Iron selenide (FeSe) is a unique material among FeSC because of its simplest structure (Fig. 1(a)) [12] and unusual electronic properties, such as strong anisotropy of the superconducting order parameter, extended electronic nematic phase, and highly tunable  $T_c$  [9]. In particular, different from iron pnictides, which has a collinear antiferromagnetic (AF) ground state below the tetragonal-to-orthorhombic structural (nematic) phase transition  $T_s$ , FeSe exhibits a similar nematic transition ( $T_s \approx 90$  K) [13], but has no static AF order, providing a broad temperature range below  $T_s$  as an ideal platform for investigating the electronic nematicity and its interplay with superconductivity.

FeSe consists of stacked charge-neutral FeSe layers (Fig. 1(a)). Upon cooling, it undergoes a nematic transition at  $T_s \approx 90$  K, below which twin domains form along two mutually perpendicular directions and exhibit macroscopic four-fold symmetry, impeding the study of the intrinsic electronic properties of the orthorhombic (nematic) state. Through detwinning FeSe using uniaxial strain, resistivity and electronic structure measurements reveal strong electronic anisotropy in the nematic state [14, 15]. At lower temperature, FeSe enters a superconducting ground state with  $T_c \approx 9$  K, in which a superconducting energy gap anisotropy has been observed via angle resolved photoemission spectroscopy (ARPES) [16] and scanning tunnelling spectroscopy (STM) [17].

In the presence of orbital splitting (or orbital ordering) between  $d_{xz}$  and  $d_{yz}$  orbitals [15, 19, 20], and the absence of magnetic order, the electronic nematic phase was suggested to be driven by orbital fluctuations [21–24]. On the other hand, various experimental evidences, in particular the discovery of intense magnetic excitations and their correlation with the nematic transition [25–27], emphasized the importance of the spin degree of freedom in driving the electronic nematic order. In addition, various localized models based on quantum paramagnetism, spin frustration and magnetic quadrupolar order were also proposed to account for the nematic transition, the magnetic excitations, and the absence of AF order [28–31].

It is proposed that resolving the intrinsic magnetic excitations in twin-free FeSe is the key for clarifying the microscopic origin of the unusual electronic anisotropy in both the superconducting and nematic state [5, 6, 39]. Through employing  $\text{BaFe}_2\text{As}_2$  as substrate for applying uniaxial strain, some of us have recently measured the low-energy spin fluctuations ( $E \lesssim 10$  meV) of detwinned FeSe using inelastic neutron scattering [32]. These results have revealed anisotropic spin fluctuations in the normal state and a spin resonance appearing at only  $\mathbf{Q}_1 = (1, 0)$  below  $T_c$ , consistent with the picture of orbital-selective Cooper pairing [17, 18]. However, neutron scattering experiments were unable to determine what happens to the

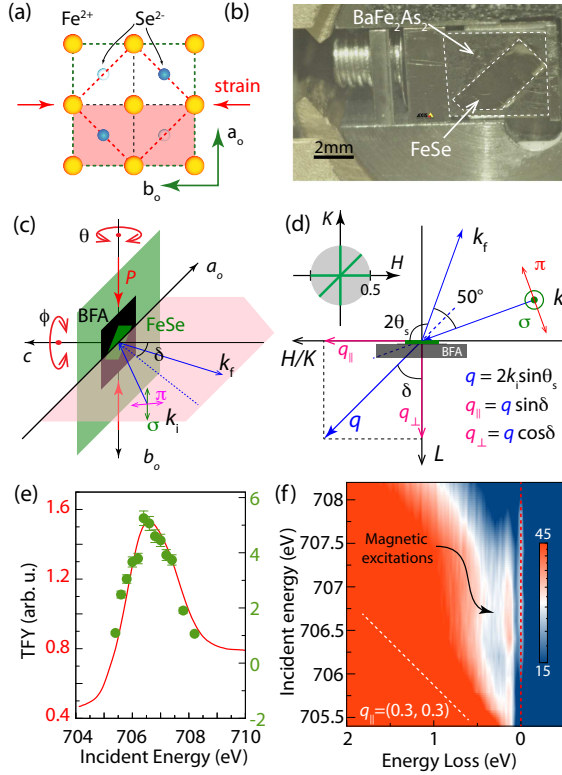


FIG. 1: Crystal structure, detwinning strategy, scattering geometry and incident energy dependent RIXS. (a) Structure of FeSe layer. FeSe crystal consists of stacked FeSe layers. The yellow filled circles mark Fe<sup>2+</sup> ions. The filled and open blue circles denote Se<sup>2-</sup> ions above and below Fe-Fe plane, respectively. The horizontal arrows mark the direction of uniaxial strain. The red dashed diamond and green dashed square denote the tetragonal and orthorhombic unit cell, respectively. (b) Detwinning strategy for FeSe. A thin FeSe crystal is glued onto a pre-cleaved BaFe<sub>2</sub>As<sub>2</sub> single crystal that is pressured in a mechanical detwinning device. Below  $T_s \approx 138$  K, the BaFe<sub>2</sub>As<sub>2</sub> crystal is detwinned and can transfer the uniaxial strain to FeSe. (c)-(d) Scattering geometry for RIXS measurements. The sample rotation  $\theta$  around the vertical axis controls the in-plane momentum transfer  $q_{\parallel}$  and the rotation  $\phi$  around  $c$ -axis can tune the scattering plane (pink area). The gray filled circle marks the momentum area accessible in this study ( $|\mathbf{q}| \leq \approx 0.5$ ). The green lines in the gray area show the high-symmetry directions for RIXS measurements. (e) Red curve is total fluorescence yield (TFY) XAS spectrum of FeSe collected near Fe- $L_3$  edge. The green dots give the integrated intensity of the magnetic excitations shown in (f). (f) Incident-energy dependence of the excitations of FeSe at  $q_{\parallel} = (0.3, 0.3)$ , measured near the Fe- $L_3$  edge with  $\pi$  polarization at  $T = 20$  K. The magnetic excitations are marked by a curved arrow.

49 magnetic excitation anisotropy across the nematic transition due to large background scattering on warming  
 50 to  $T_s$ . In addition, the energy scale of the magnetic anisotropy is unknown because the background mag-  
 51 netic scattering from the BaFe<sub>2</sub>As<sub>2</sub> substrate overwhelms the magnetic signal from FeSe for energies above  
 52 10 meV [32].

An ideal method to probe the intrinsic magnetic excitations of FeSe is to use RIXS at the Fe- $L_3$  edge in combination with the above described detwinning method (Fig. 1(b)) [33–35, 37, 38]. Since Fe- $L_3$  X-ray (707eV) penetrates less than 100nm in FeSe, while the typical thickness of a cleaved FeSe single crystal is  $\sim 20\mu\text{m}$ , RIXS studies of FeSe are free from signal contamination due to BaFe<sub>2</sub>As<sub>2</sub> and provide a unique opportunity for measuring high-energy magnetic excitations on detwinned FeSe with high efficiency.

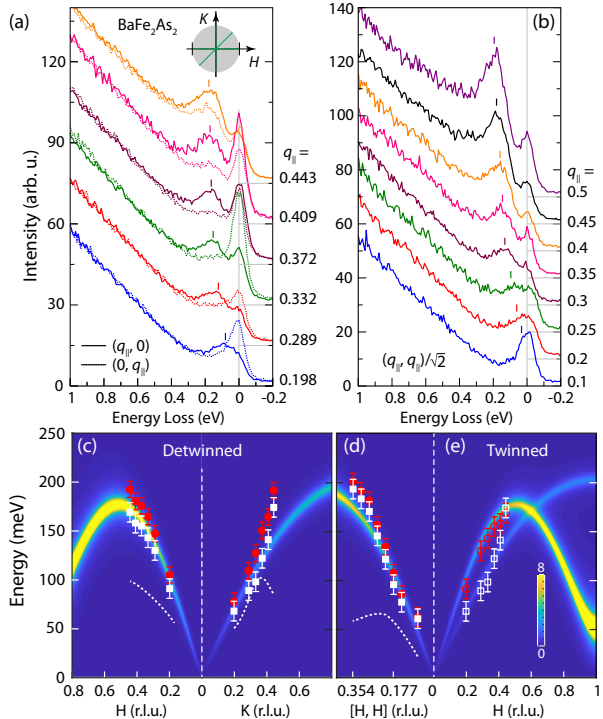


FIG. 2: Summary of RIXS results on detwinned BaFe<sub>2</sub>As<sub>2</sub>. (a) Momentum dependent RIXS spectra along  $H$  (solid lines) and  $K$  (dashed lines) directions, which are identical in a twinned crystal. (b) RIXS spectra measured along  $[H, H]$  direction. (c)-(e) Comparison between dispersions of the magnetic excitations measured with RIXS and a simulation with an extended Heisenberg model for BaFe<sub>2</sub>As<sub>2</sub> [40]. The red solid circles, white solid squares, and white dashed curves in (c) and (d) are undamped energies ( $E_0$ ), energies for the intensity maxima ( $E_m$ ), and damping factor ( $\gamma/2$ ) fitted from the spectra shown in (a) and (b) with Eq. (1). The open symbols in (e) mark the  $E_m$ .

In this work, we use RIXS to measure the intrinsic spin excitations of BaFe<sub>2</sub>As<sub>2</sub> and FeSe along high symmetry directions  $H$ ,  $K$  and  $[H, H]$ , denoted by  $S_h(q_{||})$ ,  $S_k(q_{||})$  and  $S_{hh}(q_{||})$ , respectively. To facilitate discussions, we define the spin excitations associated with  $\mathbf{Q}_1 = (1, 0)$  as  $S_1(q, E)$  and that associated with  $\mathbf{Q}_2 = (0, 1)$  as  $S_2(q, E)$ . The ratio between  $S_h(q_{||})$  and  $S_k(q_{||})$ ,  $\psi(q_{||}) = S_h(q_{||})/S_k(q_{||})$ , directly probes the spin-excitation unbalance between  $S_1$  and  $S_2$ , which is commonly termed nematic spin correlations in the nematic ordering and fluctuating region [39–41]. We denote the momentum transfer in reciprocal lattice unit (r.l.u.) (See Experimental Setups in Methods). Our results reveal that the spin-excitation anisotropy

in detwinned FeSe manifests over a large energy range up to 200 meV. It persists up to a temperature slightly above  $T_s$ , before fading away at a temperature well above  $T_s$ . Its comparison with the intrinsic spin-wave anisotropy of BaFe<sub>2</sub>As<sub>2</sub> establishes strong nematic spin correlations in both energy scale and amplitude in FeSe. This strong spin-excitation anisotropy establishes a direct connection with the nematic phase, suggesting that the nematic order is primarily spin-driven because the energy range of the nematic-phase-induced spin excitation anisotropy is much larger than that of orbital order [20–22]. Furthermore, our results identify dispersive high-energy spin excitations that are underdamped, which is highly peculiar for a paramagnet, but can be understood from a local-moment based model with antiferro-quadrupolar order [29]. As such, our results provide much-needed new insights into the mechanism for the nematicity of FeSe.

RIXS at transition-metal  $L$  edges has been widely used to study the (para)magnons of cuprate and FeSCs [33–35, 37, 38, 42–45], as well as various elementary excitations including phonon, crystal-field excitations and plasmons [43, 46]. Figure 1(b) shows a FeSe crystal prepared for RIXS measurements, which is glued onto a square-shaped BaFe<sub>2</sub>As<sub>2</sub> sample with the same orientation. Uniaxial pressure is applied on BaFe<sub>2</sub>As<sub>2</sub> along the tetragonal [110] direction (orthorhombic  $b$  axis). Upon cooling, BaFe<sub>2</sub>As<sub>2</sub> will be detwinned below  $T_s \approx 138$ K and generates an orthorhombic distortion  $\delta = (a-b)/(a+b) = 0.36\%$  that can be transferred to and thereby detwin FeSe below its structural transition at  $T_s \approx 90$ K. Figs. 1(c) and 1(d) illustrate the scattering geometry, the substantial area of the first Brillouin zone accessible with Fe- $L_3$  RIXS, and calculation of the in-plane momenta  $q_{||}$ .

We first carried out incident-energy dependent RIXS (energy detuning) measurements for both BaFe<sub>2</sub>As<sub>2</sub> and FeSe around their resonating energies which are determined by x-ray absorption spectra (XAS) (Fig. 1(e)). Figure 1(f) shows a RIXS map for an unstrained FeSe sample measured at  $q_{||} = (0.3, 0.3)$  with  $\pi$  polarisation and  $T = 20$ K. While fluorescence and particle-hole excitations dominate the scattering signal above  $\sim 0.5$  eV, a clear intrinsic elementary excitation (Raman mode) is observed at  $\sim 160$ meV well separated from the fluorescence peak setting on above  $\sim 200$ meV. The integrated intensity of this Raman mode (green dots in Fig. 1(e)) follows the XAS (red curve in Fig. 1(e)), indicating the cross section is enhanced near the Fe- $L_3$  edge. In addition, phonon contribution to this mode can also be excluded because of its much smaller energy scale ( $\sim 40$  meV) [37]. Taking together the intrinsic spin-wave dispersion of detwinned BaFe<sub>2</sub>As<sub>2</sub> being consistent with that measured by neutron scattering and RIXS (Fig. 2) [33, 33–38, 40, 47], and the dispersive nature of the excitations observed in detwinned FeSe (Fig. 3), we conclude that the dispersive collective excitations present in Figs. 2 and 3 are single spin-flip magnetic excitations in the first Brillouin zone [33, 37, 38].

To determine the spin-excitation anisotropy in FeSe, we take BaFe<sub>2</sub>As<sub>2</sub> as a reference, in which intrinsic spin waves ( $T < T_N$ ) and nematic spin correlations are carefully investigated using RIXS here and can

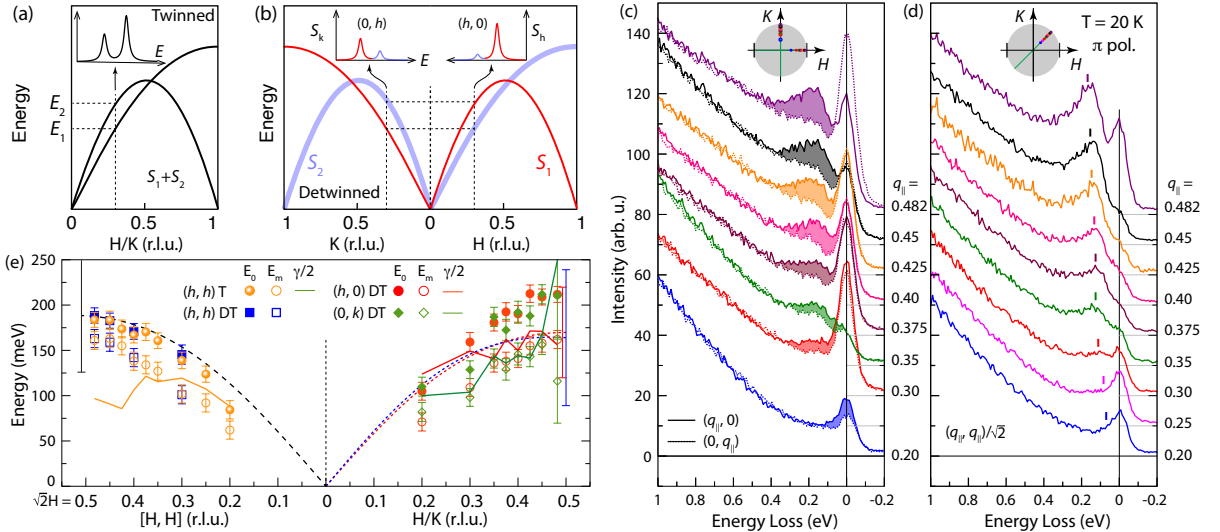


FIG. 3: Schematic of magnetic excitation dispersions for (a) twinned and (b) detwinned FeSe assuming difference between  $S_2$  and  $S_1$ . Correspondingly, the insets in (a) and (b) show schematic RIXS energy spectra for twinned and detwinned FeSe. (c), (d) Momentum-dependent RIXS spectra of (c) detwinned FeSe along  $H/K$  and (d) twinned FeSe along  $[H, H]$  directions. The colored area mark the difference between  $S_h(q_{\parallel})$  and  $S_k(q_{\parallel})$ . The colored dots in the insets mark the momenta where spectra were collected. (e) Energy dispersions obtained from the fitting of the RIXS spectra in (c) and (d) with Eq. (1). The solid (open) red circles, green diamonds, orange circles, and blue squares mark the undamped energies  $E_0$  (energies for intensity maxima  $E_m$ ) of the dispersions along  $H$  (detwinned),  $K$  (detwinned),  $[H, H]$  (twinned), and  $[H, H]$  (detwinned) directions, respectively. The red, green and orange lines mark the momentum-dependent damping factor  $\gamma/2$  along high symmetry directions. The black, red, and blue dashed curves are the calculated flavor-wave dispersions in the AFQ phase along  $[H, H]$  and  $H/K$  directions, respectively. The errorbars mark the damping factor  $\gamma/2$  along the corresponding directions.

be compared to previous neutron scattering studies of detwinned samples [40]. Figure 2 summarizes the RIXS results on a 100% detwinned  $\text{BaFe}_2\text{As}_2$ . Highly dispersive magnetic excitations  $S_h$ ,  $S_k$  (Fig. 2(a)), and  $S_{hh}$  (Fig. 2(b)) along three high-symmetry directions  $H$ ,  $K$  and  $[H, H]$  are resolved, respectively. While twinned  $\text{BaFe}_2\text{As}_2$  is expected to show four-fold symmetric magnetic excitations [33, 47] ( $S_h(q_{\parallel}) = S_k(q_{\parallel})$ ), detwinned  $\text{BaFe}_2\text{As}_2$  exhibits highly anisotropic excitations along  $H$  and  $K$  due to an inherent difference in the spin-wave branches along these two directions [40]. The ratio between  $S_h(q_{\parallel})$  and  $S_k(q_{\parallel})$  — the spin excitation anisotropy, increases with  $q_{\parallel}$  up to 0.409 but decreases at higher  $q_{\parallel} = 0.443$  (Fig. 2(a)), revealing a non-monotonic momentum dependence.

In order to obtain the dynamic structure factor for the magnetic excitations, we use a general damped

harmonic oscillator model [33–35, 37]

$$S(q, E) = A \frac{E_0}{1 - e^{-\beta E}} \frac{2 \gamma E}{(E^2 - E_0^2)^2 + (E \gamma)^2}, \quad (1)$$

to fit the magnetic excitations, in which  $E_0$  is the undamped energy and  $\gamma$  the damping factor. The elastic peak can be fitted with a Gaussian function, and the fluorescence contributions below  $\sim 1$  eV can be described with a quadratic polynomial [48]. The fitting results, the undamped energy dispersion ( $E_0(q)$ , red solid circles), the energies for the intensity maxima ( $E_m(q)$ , white solid squares), and the damping factor ( $\gamma/2$ , white dashed curves) are over-plotted onto the simulation of the spin waves based on an anisotropic Heisenberg  $J_{1a} - J_{1b} - J_2 - J_c$  model described in ref. [47] (Fig. 2(c)), in which we set  $L = 0$  because the spin waves of BaFe<sub>2</sub>As<sub>2</sub> are two dimensional, especially at the high-energies probed in our RIXS measurements. We find  $E_0 > \gamma/2$  at all the momenta measured, which indicates that the spin waves are underdamped and far from being critically damped. Note the damping rates  $\gamma(q)$  are highly anisotropic in  $[H, K]$  space. The damping along  $K$  direction is apparently larger than that along  $H$  and  $[H, H]$  directions. The intrinsic spin waves of the clearly resolved two different branches  $S_h(q)$  and  $S_k(q)$  around  $\Gamma$  is consistent with the anisotropic Heisenberg model, in which dispersive spin waves can only arise from the AF wave vector  $\mathbf{Q}_1$  ( $S_1$ ). The minor deviation of the branch  $S_k(q)$  from the anisotropic Heisenberg model can be attributed to the failure of the anisotropic Heisenberg model in describing the small anisotropy of magnetic excitations at high energy, due to the emergence of the spin excitations around  $\mathbf{Q}_2 = (0, 1)$  ( $S_2$ ) at  $E \gtrsim 100$  meV observed by neutron scattering [40, 41].

Having reproduced the intrinsic spin waves of detwinned BaFe<sub>2</sub>As<sub>2</sub>, we move to the RIXS study of detwinned FeSe. The schematics in Figs. 3(a) and 3(b) illustrate the principle for resolving nematic spin correlations in the first Brillouin zone [48]. In a twinned sample with anisotropic excitations, RIXS measurements generate  $S_h = S_k$  (black curve in the inset of Fig. 3(a)). Both  $S_h$  and  $S_k$  consist of two spin-excitation branches from  $S_1$  and  $S_2$  in twin domains, where we assume  $S_1$  and  $S_2$  have the same energy dispersion for simplicity. For a detwinned sample,  $S_1$  and  $S_2$  will also be present along both  $H$  and  $K$  directions (Fig. 3(b)) with *different* spectral weight, for which the ratio between  $S_h$  and  $S_k$  reflects the nematic spin correlations [48].

Momentum-dependent RIXS of FeSe collected at  $T = 20$  K  $< T_s$  are summarized in Figs. 3(c) and 3(d). Figure 3(c) displays magnetic excitations along  $H$  ( $S_h$ , solid curves) and  $K$  ( $S_k$ , dashed curves) directions, and Fig. 3(d) along  $[H, H]$  ( $S_{hh}$ ) directions. While all the spin excitations show considerable damping, the peaks along  $[H, H]$  are more pronounced than for  $H$  and  $K$ , indicating less damping along  $[H, H]$ . Figure 3(c) reveals significant difference between  $S_h(q_{||})$  and  $S_k(q_{||})$  at all  $q_{||}$  (colored area in Fig. 3(c)), and therefore demonstrates the existence of high energy spin-excitation anisotropy (nematic spin correlations)

in the nematic state of detwinned FeSe. Compared with  $\text{BaFe}_2\text{As}_2$  where the difference between  $S_h$  and  $S_k$  drops at high  $q_{||} = 0.443$  (Fig. 2(a)), the difference in FeSe (colored area in Fig. 3(c)) retains a large amplitude at an even higher  $q_{||} = 0.482$ .

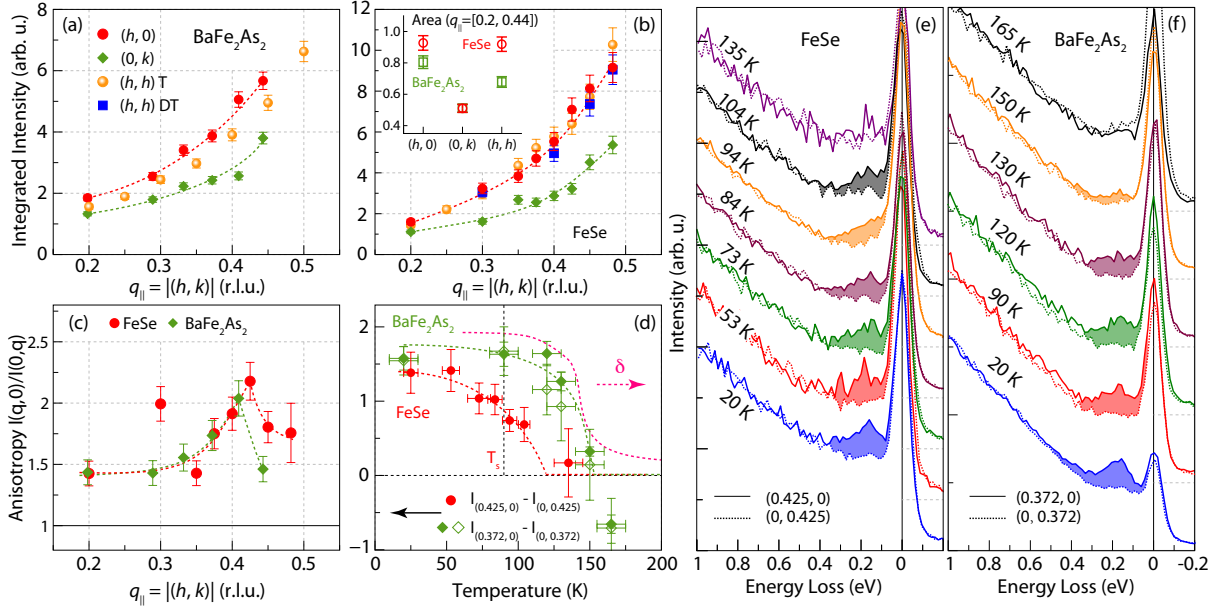


FIG. 4: Anisotropic magnetic excitations in detwinned  $\text{BaFe}_2\text{As}_2$  and FeSe. (a), (b) Momentum-dependent energy-integrated intensity of magnetic excitations for  $\text{BaFe}_2\text{As}_2$  and FeSe. The inset shows the momentum-integrated intensity of  $S_{h/k/hh}$  for  $\text{BaFe}_2\text{As}_2$  (green squares) and FeSe (red circles) in the range of  $q_{||} = [0.2, 0.44]$ . (c) Spin excitation anisotropy between  $S_h$  and  $S_k$ , defined as the ratio between the integrated intensity for  $(q, 0)$  and  $(0, q)$  as shown in (a) and (b). (d) Temperature dependence of the spin-excitation difference between  $S_h(q_{||})$  and  $S_k(q_{||})$ , in which the data points are integrated intensity of  $S_h(q_{||}) - S_k(q_{||})$  in the energy range of  $[0.08, 0.4]$  eV as shown in (e) and (f). The dashed lines in (c) and (d) are guides to the eye. The pink dashed curve shows the lattice distortion  $\delta = (a - b)/(a + b)$  of  $\text{BaFe}_2\text{As}_2$  under a uniaxial pressure of  $\sim 20$  MPa, which reaches 0.36% below  $\sim 100$  K. The vertical black dashed line marks the  $T_s = 90$  K for FeSe. (e), (f) Temperature-dependent RIXS spectra for FeSe and  $\text{BaFe}_2\text{As}_2$  measured at  $q_{||} = 0.425$  and  $0.372$ , respectively. The colored areas in (e) and (f) mark the intensity difference between  $S_h(q_{||})$  and  $S_k(q_{||})$ .

In order to achieve a quantitative characterization of the nematic spin correlations in FeSe, we use the same fitting model as for  $\text{BaFe}_2\text{As}_2$  to extract the energy dispersion and the integrated intensity of the magnetic excitations  $S_h$ ,  $S_k$  and  $S_{hh}$ . Figure 3(e) shows the energy dispersions obtained from the fitting of the magnetic excitations shown in Figs. 3(c) and 3(d). The solid symbols mark the bare energy dispersions ( $E_0$ ) without damping effect, and the open symbols represent the energy dispersions for the intensity maxima  $E_m$ . The momentum-dependent damping factors  $\gamma/2$  are overall larger than that for  $\text{BaFe}_2\text{As}_2$  but still in the underdamped regime for most of the excitations. Moreover, the damping factor

for  $S_{hh}$  (along  $[H, H]$  direction) is smaller than for  $S_{h/k}$  in both  $\text{BaFe}_2\text{As}_2$  and FeSe, suggesting a common anisotropic damping effect in FeSC. The (anisotropic) unerdamped nature of the magnetic excitations, not inferable in previous neutron scattering and RIXS studies on twinned samples [26, 37], which favors a local moment picture with strong electron correlation, can now be conclusively revealed and discussed.

Since the largest momentum  $(0.482, 0)$  along  $H$  is close to the zone boundary  $(0.5, 0)$ , the excitation energy scale of FeSe ( $E_0 \sim 200$  meV and  $E_m \sim 160$  meV) at  $(0.482, 0)$  and  $(0, 0.482)$  (consistent with that in ref. [37]) reveals a much higher band top in the first BZ than that ( $\sim 120 - 150$  meV) observed by neutron scattering in the BZ around  $(1, 0)$  [26]. This is in stark contrast to the case of  $\text{BaFe}_2\text{As}_2$  where the dispersions measured by RIXS and neutron scattering can be consistently described with one model (Fig. 2) [33, 40]. We attribute this difference to the absence of stripe AF order in FeSe. Because of the translational symmetry of the stripe AF order ( $\mathbf{k} = (1, 0)$ ) in  $\text{BaFe}_2\text{As}_2$ , the magnetic excitations in the first BZ can be deemed as a replica of that in the BZ centering at  $\mathbf{Q} = (1, 0)$ . However, long range AF order is not established in spite of the strong in-plane magnetic correlations in FeSe. Thus the dispersions around  $\Gamma$  and  $(1, 0)$  do not have to be identical. However, how to quantitatively reconcile the neutron scattering and RIXS results is still an open question.

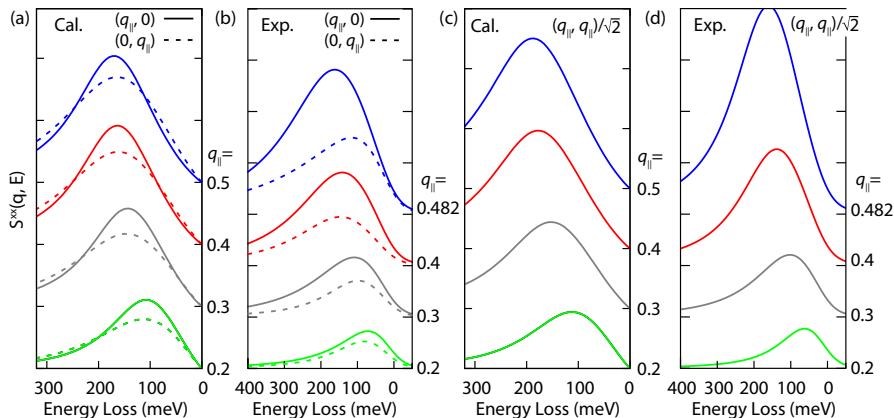


FIG. 5: Calculated spin excitation spectra of the AFQ phase and their comparison with the fitting curve of the  $S(q_{\parallel})$ . (a), (c) Calculated spectra along (a) the  $H/K$  directions, and (c) the  $[H, H]$  direction. (b), (d) Fitting curves of the  $S(q_{\parallel})$  along (b) the  $H/K$  directions and (d)  $[H, H]$  direction.

Figures 4(a) and 4(b) shows the momentum-dependent energy-integrated intensity of the spin excitations  $S_h$ ,  $S_k$  and  $S_{hh}$  for  $\text{BaFe}_2\text{As}_2$  and FeSe, respectively. With increasing  $q_{\parallel}$ , the integrated intensities along all the three high symmetry directions increase monotonically. It is also found that the spin-excitation intensity for FeSe is slightly higher than  $\text{BaFe}_2\text{As}_2$ , qualitatively consistent with previous neutron scattering results [26]. Note the momentum-direction dependence of the amplitude for  $S_{h/k/hh}$  is modulated by the anisotropic damping factor inherent to  $S_{1,2}$ , which require  $S_{1,2} = 0$  at  $\Gamma$  [47]. To quantify the

spin-excitation anisotropy, we plot the ratio  $I_{(q,0)}/I_{(0,q)} = S_h/S_k$  for FeSe and BaFe<sub>2</sub>As<sub>2</sub> in the same panel (Fig. 4(c)). It is surprising that the spin-excitation anisotropy of FeSe (reflecting the nematic spin correlation) is rather similar to the spin-wave anisotropy of BaFe<sub>2</sub>As<sub>2</sub> in both amplitude and energy scale. Furthermore, at high-energy/momentum region, the anisotropy of FeSe is even larger than for BaFe<sub>2</sub>As<sub>2</sub>. This prominent spin-excitation anisotropy signifies strong electronic nematicity with large energy scale ( $\sim 200$  meV) and magnitude in FeSe. Moreover, the temperature dependence of the difference between  $S_h$  and  $S_k$  for FeSe at selected  $q_{\parallel} = 0.425$  decreases with increasing temperature, persists to a temperature (104 K) 20% higher than  $T_s$  and finally drastically reduces at a temperature (135 K) well above  $T_s$ , indicating a gradual suppression of nematic spin correlations above  $T_s$  (Figs. 4(d) and 4(e)). Since FeSe is under uniaxial strain applied from the BaFe<sub>2</sub>As<sub>2</sub> substrate (pink dashed curve in Fig. 4(d)),  $T_s$  is no longer well defined. For this reason, it is not surprising that spin-excitation anisotropy disappears at a temperature above the zero pressure  $T_s$ . This temperature dependence is similar to that for BaFe<sub>2</sub>As<sub>2</sub> as shown in Figs. 4(d) and 4(f), in which the anisotropy at  $q_{\parallel} = 0.372$  persists at a temperature slightly higher than  $T_N$  but vanishes at  $T = 165$  K.

Previous measurements of the spin dynamics in the detwinned FeSe were constrained to low energies ( $\lesssim 10$  meV) [32], and were unable to discriminate between the different scenarios for the nematicity in FeSe. Our measurements here over a large energy window enables the discovery that the detwinned FeSe harbors high-energy (up to 200 meV) anisotropic spin excitations that are dispersive and underdamped. This surprising finding is at a striking variance with the itinerant mechanism for the nematicity in FeSe, in which even the spin excitations at such high energies are highly overdamped [51].

Instead, the dispersive and underdamped nature of the spin excitations point to a local-moment starting point to describe the nematicity. This has led us to consider a generalized bilinear-biquadratic model on a square lattice with local moments. We have calculated the spin dynamics in the proposed picture for the nematicity based on a (1, 0) antiferroquadrupolar state [29]; the details are given in the Supplementary Information. In Fig. 5, we show that the calculated spin dynamics provide a good understanding of the experimental data. Thus, our results provide evidence for a local-moment-based picture for the nematicity of FeSe.

Our work brings about a remarkable degree of universality across the Fe-based superconductors. For BaFe<sub>2</sub>As<sub>2</sub> with collinear AF order, the anisotropy can be readily interpreted in the picture of intrinsic spin waves [40, 41]. FeSe, by contrast, lacks long-range magnetic order even though it is nematic. The local-moment-based understanding, as dictated by the qualitative similarities in the high energy spin excitations between FeSe and BaFe<sub>2</sub>As<sub>2</sub>, suggest that the largest spin spectral weight is associated with the incoherent electronic excitations induced by the underlying electron correlations. As such, our work not only allows

200 for discriminating the proposed mechanisms for the nematicity of FeSe but also points to a unified under-  
 201 standing of the correlation physics [36] across the seemingly distinct classes of Fe-based superconductors.

---

202 \* Electronic address: luxy@bnu.edu.cn

203 † Electronic address: pdai@rice.edu

204 ‡ Electronic address: thorsten.schmitt@psi.ch

- 205 [1] Fradkin, E., Kivelson, S. A., & Tranquada, J. M., Colloquium: Theory of intertwined orders in high temperature  
 206 superconductors. Rev. Mod. Phys. **87**, 457 (2015).
- 207 [2] Chu, J.-H. *et al.* In-plane resistivity anisotropy in an underdoped iron arsenide superconductor. Science **329**,  
 208 824-826 (2010).
- 209 [3] Yi, M. *et al.* Symmetry-breaking orbital anisotropy observed for detwinned  $\text{Ba}(\text{Fe}_{1-x}\text{Co}_x)_2\text{As}_2$  above the spin  
 210 density wave transition. Proc. Natl Acad. Sci. USA **108**, 6878-6883 (2011).
- 211 [4] Chu, J.-H., Kuo, H.-H., Analytis, J. G., & Fisher, I. R. Divergent Nematic Susceptibility in an Iron Arsenide  
 212 Superconductor, Science **337**, 710 (2012).
- 213 [5] Fernandes, R. M., Chubukov, A. V. & Schmalian, J. What drives nematic order in iron-based superconductors?  
 214 Nat. Phys **10**, 97-104 (2014).
- 215 [6] Si, Q., Yu, R. & Abrahams, E, Hightemperature superconductivity in iron pnictides and chalcogenides, Nat. Rev.  
 216 Mater. **1**, 16017 (2016).
- 217 [7] Kuo, H.-H., Chu, J.-H., Palmstrom, J. C., Kivelson, S. A., & Fisher, I. R. Ubiquitous signatures of nematic  
 218 quantum criticality in optimally doped Fe-based superconductors. Science **352**, 958-962 (2016).
- 219 [8] Böhmer, A. E. & Meingast, C. Electronic nematic susceptibility of iron-based superconductors. C. R. Physique  
 220 **17** 90-112 (2016).
- 221 [9] Böhmer, A. E. & Kreisel, A., Nematicity, magnetism and superconductivity in FeSe. J. Phys.: Condens. Matter  
 222 **30**, 023001 (2018).
- 223 [10] Metlitski, M. A. *et al.* Cooper pairing in non-Fermi liquids. Phys. Rev. B **91**, 115111(2015).
- 224 [11] Lederer, S. *et al.* Enhancement of Superconductivity near a Nematic Quantum Critical Point. Phys. Rev. Lett.  
 225 **114**, 097001 (2015).
- 226 [12] Hsu, F. C. *et al.* Superconductivity in the PbO-type structure  $\alpha$ -FeSe. Proc. Natl Acad. Sci. USA **105**, 14262  
 227 (2008).
- 228 [13] McQueen, T. M. *et al.* Tetragonal-to-orthorhombic structural phase transition at 90K in the superconductor  
 229  $\text{Fe}_{1.01}\text{Se}$ . Phys. Rev. Lett. **103**, 057002 (2009).
- 230 [14] Tanatar, M. A. et al., Origin of resistivity anisotropy in the nematic phase of FeSe, Phys. Rev. Lett. **117**, 127001  
 231 (2016).
- 232 [15] Coldea, A. & Watson M. D., The key ingredients of the electronic structure of FeSe, Annu. Rev. Condens. Matter  
 233 Phys. **9**, 125-146 (2018).

- [16] Liu, D. F. *et al.* Orbital origin of extremely anisotropic superconducting gap in nematic phase of FeSe superconductor. *Phys. Rev. X* **8**, 031033 (2018).
- [17] Sprau, P. O. *et al.* Discovery of orbital-selective Cooper pairing in FeSe, *Science* **357**, 75-80 (2017).
- [18] R. Yu, Zhu, J.-X. & Si, Q., Orbital-selective superconductivity, gap anisotropy and spin resonance excitations in a multiorbital  $t$ - $J_1$ - $J_2$  model for iron pnictides. *Phys. Rev. B* **89**, 024509 (2014).
- [19] Lee, C. C., Yin, W.-G., & Ku, W., Ferro-orbital order and strong magnetic anisotropy in the parent compounds of iron-pnictide superconductors, *Phys. Rev. Lett.* **103**, 267001 (2009).
- [20] Yi, M. *et al.* The nematic energy scale and the missing electron pocket in FeSe, *Phys. Rev. X* **9**, 041049 (2019).
- [21] Baek, S.-H. *et al.* Orbital-driven nematicity in FeSe. *Nat. Mater.* **14**, 210 (2015).
- [22] Böhmer, A. E. *et al.* Origin of the tetragonal-to-orthorhombic phase transition in FeSe: A combined thermodynamic and NMR study of nematicity. *Phys. Rev. Lett.* **114**, 027001 (2015).
- [23] Yamakawa, Y., Onari, S., & Kontani, H. Nematicity and magnetism in FeSe and other families of Fe-based superconductors, *Phys. Rev. X* **6**, 021032 (2016).
- [24] Onari, S., Yamakawa, Y., & Kontani, H. Sign-reversing orbital polarization in the nematic phase of FeSe due to the  $C_2$  symmetry breaking in the self-energy, *Phys. Rev. Lett.* **116**, 227001 (2016).
- [25] Wang, Q. *et al.* Strong interplay between stripe spin fluctuations, nematicity and superconductivity in FeSe. *Nat. Mater.* **15**, 159 (2016).
- [26] Wang, Q. *et al.* Magnetic ground state of FeSe. *Nat. Commun.* **7**, 12182 (2016).
- [27] Ma, M. W. *et al.* Prominent role of spin-orbit coupling in FeSe revealed by inelastic neutron scattering, *Phys. Rev. X* **7**, 021025 (2017).
- [28] Wang, F., Kivelson, S. & Lee, D.-H. Nematicity and quantum paramagnetism in FeSe. *Nat. Phys.* **11**, 959-963 (2015).
- [29] Yu, R. & Si, Q. Antiferroquadrupolar and Ising-nematic orders of a frustrated bilinear-biquadratic Heisenberg model and implications for the magnetism of FeSe. *Phys. Rev. Lett.* **115**, 116401 (2015).
- [30] Glasbrenner, J. K. *et al.* Effect of magnetic frustration on nematicity and superconductivity in iron chalcogenides. *Nat. Phys.* **11**, 953 (2015).
- [31] She, J.-H., Lawler, M. J., & Kim, E.-A., Quantum spin liquid intertwining nematic and superconducting order in FeSe, *Phys. Rev. Lett.* **121**, 237002 (2018).
- [32] Chen, T. *et al.*, Anisotropic spin fluctuations in detwinned FeSe. *Nat. Mater.* **18**, 709-716 (2019).
- [33] Zhou, K. *et al.*, Persistent high-energy spin excitations in iron-pnictide superconductors. *Nat. Commun.* **4**, 1470 (2013).
- [34] Pelliciari *et al.*, Local and collective magnetism of EuFe<sub>2</sub>As<sub>2</sub>. *Phys. Rev. B* **95**, 115152 (2017).
- [35] Garcia, F. A. *et al.*, Anisotropic magnetic excitations and incipient Néel order in Ba(Fe<sub>1-x</sub>Mn<sub>x</sub>)<sub>2</sub>As<sub>2</sub>. *Phys. Rev. B* **99**, 115118 (2019).
- [36] Pelliciari, J. *et al.*, Reciprocity between local moments and collective magnetic excitations in the phase diagram of BaFe<sub>2</sub>(As<sub>1-x</sub>P<sub>x</sub>)<sub>2</sub>. *Communications Physics* **2**, 139 (2019).
- [37] Rahn, M. C. *et al.*, Paramagnon dispersion in  $\beta$ -FeSe observed by Fe *L*-edge resonant inelastic x-ray scattering,

- 271 Phys. Rev. B **99**, 014505 (2019).
- 272 [38] Pelliciari, J. *et al.*, Evolution of spin excitations from bulk to monolayer FeSe, Nature Communications **12**, 3122  
273 (2021).
- 274 [39] Lu, X. *et al.*, Nematic spin correlations in the tetragonal state of uniaxial-strained BaFe<sub>2-x</sub>Ni<sub>x</sub>As<sub>2</sub>, Science **345**,  
275 657 (2014).
- 276 [40] Lu, X. *et al.*, Spin waves in detwinned BaFe<sub>2</sub>As<sub>2</sub>, Phys. Rev. Lett. **121**, 067002 (2018).
- 277 [41] Liu, C. *et al.*, Anisotropic magnetic excitations of a frustrated bilinear-biquadratic spin model – Implications for  
278 spin waves of detwinned iron pnictides. Phys. Rev. B **101**, 024510 (2020).
- 279 [42] Ament, L. J. P. *et al.*, Resonant inelastic x-ray scattering studies of elementary excitations. Rev. Mod. Phys. **83**,  
280 705 (2011).
- 281 [43] Schlappa, J. *et al.*, Spin-orbital separation in the quasi-one-dimensional Mott insulator Sr<sub>2</sub>CuO<sub>3</sub>. Nature **485**,  
282 82-85 (2012).
- 283 [44] Peng, Y. Y. *et al.*, Influence of apical oxygen on the extent of in-plane exchange interaction in cuprate supercon-  
284 ductors. Nat. Phys. **13**, 1201 (2017).
- 285 [45] Jia, C. *et al.*, Using RIXS to uncover elementary charge and spin excitations. Phys. Rev. X **6**, 021020 (2016).
- 286 [46] Hepting, M. *et al.*, Three-dimensional collective charge excitations in electron-doped copper oxide supercon-  
287 ductors. Nature **563**, 374-378 (2018).
- 288 [47] Harriger, L. W. *et al.*, Nematic spin fluid in the tetragonal phase of BaFe<sub>2</sub>As<sub>2</sub>, Phys. Rev. B **84**, 054544 (2011).
- 289 [48] See the supplemental materials for details.
- 290 [49] Tam, D. W. *et al.* Orbital selective spin waves in detwinned NaFeAs, Phys. Rev. B **102**, 054430 (2020).
- 291 [50] Yin, Z. P. Haule, K. and Kotliar, G. Spin dynamics and orbital-antiphase pairing symmetry in iron-based super-  
292 conductors. Nat. Phys. **10**, 845-850 (2014).
- 293 [51] Kreisel, A., Andersen, B. M., & Hirschfeld, P. J. Itinerant approach to magnetic neutron scattering of FeSe:  
294 effect of orbital selectivity, Phys. Rev. B **98**, 214518 (2019).
- 295 [52] Strocov, V. N. *et al.*, High-resolution soft X-ray beamline ADRESS at the Swiss Light Source for resonant  
296 inelastic X-ray scattering and angle-resolved photoelectron spectroscopies. Journal of synchrotron radiation **17**,  
297 631-643. (2010).
- 298 [53] Ghiringhelli G. *et al.*, A high resolution spectrometer for resonant x-ray emission in the 400-1600eV energy  
299 range. Review of Scientific Instruments **77**, 113108 (2006).

### 300 Acknowledgement

301 The work at Beijing Normal University is supported by the National Natural Science Foundation of  
302 China (Grant No. 11922402 and 11734002). The RIXS experiments were carried out at the ADRESS  
303 beamline of the Swiss Light Source at the Paul Scherrer Institut. The work at PSI is supported by the  
304 Swiss National Science Foundation through project no. 200021\_178867, the NCCR MARVEL and the  
305 Sinergia network Mott Physics Beyond the Heisenberg Model (MPBH). The work at Renmin University was  
306 supported by the Ministry of Science and Technology of China, National Program on Key Research Project

307 Grant No.2016YFA0300504 and Research Funds of Remnin University of China Grant No. 18XNLG24  
 308 (R.Y.) The experimental work at Rice university is supported by the U.S. Department of Energy, BES under  
 309 Grant No. DE-SC0012311 (P.D.). The single-crystal synthesis work at Rice is supported by Robert A.  
 310 Welch Foundation Grant No. C-1839 (P.D.). The theoretical work at Rice was supported by the U.S.  
 311 Department of Energy, Office of Science, Basic Energy Sciences, under Award No. DE-SC0018197, and  
 312 the computational part by the Robert A. Welch Foundation Grant No. C-1411 (Q.S.). Work at Los Alamos  
 313 was carried out under the auspices of the U.S. DOE NNSA under Contract No. 89233218CNA000001.  
 314 It was supported by LANL LDRD Program and in part by the Center for Integrated Nanotechnologies, a  
 315 U.S. DOE BES user facility. Q.S. acknowledges the hospitality of the Aspen Center for Physics, which is  
 316 supported by NSF grant No. PHY-1607611.

317 **Methods**

318 **Sample preparation** The high-quality BaFe<sub>2</sub>As<sub>2</sub> and FeSe single crystals used in the present study were  
 319 grown using self-flux and chemical vapor transport method, respectively. The BaFe<sub>2</sub>As<sub>2</sub> single crystals were  
 320 oriented using a Laue camera and cut along tetragonal [110] and [1-10] directions using a high-precision  
 321 wire saw (WS-25). The direction of the self-cleaved edges of FeSe single crystals were also determined  
 322 using a Laue camera. The well-cut BaFe<sub>2</sub>As<sub>2</sub> crystals, with typical size 5mm×4.3mm×0.5mm, were pre-  
 323 cleaved before the final preparation. For RIXS measurements of BaFe<sub>2</sub>As<sub>2</sub>, we put a ceramic top-post onto  
 324 the upper surface of BaFe<sub>2</sub>As<sub>2</sub> for in-situ cleaving. For RIXS measurements of FeSe, we glue thin FeSe  
 325 crystals onto the upper surface of BaFe<sub>2</sub>As<sub>2</sub> along the same direction using epoxy Stycast 1266 and a small  
 326 ceramic top-post onto the surface of FeSe. The prepared crystals with the posts were inserted into the slot  
 327 of the uniaxial-pressure devices, which were mounted on a modified copper sample holder of the RIXS  
 328 spectrometer (See Fig. 1(b)).

329 **Experimental setups** The RIXS and XAS measurements were performed with the RIXS spectrometer at  
 330 ADRESS beamline of Swiss Light Source at the Paul Scherer Institut [52, 53]. The beam size at the sample  
 331 position is  $4 \times 55\mu\text{m}^2$ . All the measurements shown in the main text were collected using linear horizontal  
 332 (LH) polarization (electric field vector of the incident photons lying within the horizontal scattering plane),  
 333 denoted as  $\pi$  polarization. The RIXS spectra were collected with a grazing-incidence configuration, as  
 334 shown in Fig. 1(d). The scattering angle was set to  $2\theta_s = 130^\circ$ , by which a substantial area of the first Bril-  
 335 louin zone is accessible [gray circle in Fig. 1(d)]. The measurements were performed along high-symmetry  
 336 directions  $H/K$  and  $[H, H]$  in orthorhombic notation. The total energy resolution for the RIXS measure-  
 337 ments was set to 80 meV. The in-plane momentum  $q_{||}$  can be tuned continuously by rotating the sample  
 338 and thereby changing the angle ( $\delta$ ). Before measurements, the sample holder was inserted into the manip-  
 339 ulator head and the top-post was removed by cleaving at low temperature ( $\sim 20\text{K}$ ) and ultra-high vacuum

340 ( $< 10^{-10}$  mbar). Through the experiments, we define reciprocal lattice unit as  $(q_x a_o / 2\pi, q_y b_o / 2\pi, q_z c / 2\pi)$   
341 with  $a_o \approx 5.334\text{\AA}$ ,  $b_o \approx 5.308\text{\AA}$  and  $c \approx 5.486\text{\AA}$ . The FeSe tri-layer height is  $d \approx 5.5\text{\AA}$ . The orthorhombic  
342 lattice distortion of FeSe is  $\delta = (a_o - b_o) / (a_o + b_o) \approx 0.27\%$  at a temperature well below  $T_s$ .

343 **Author contributions**

344 X.L. conceived this project and developed the detwinning strategy. X.L. and T.S. wrote the beamtime  
345 proposals and coordinated together the experiments as well as all other project phases. X.L., W.Z., Y.T.,  
346 E.P., R.L., Z.T., and T.S. carried out the RIXS experiments. P.L., R.L., and Z.T. prepared the BaFe<sub>2</sub>As<sub>2</sub>  
347 single crystals. T.C. and P.D. provided the FeSe single crystals. R.Y. and Q.S. carried out theoretical and  
348 computational analyses. X.L., P.D., and T.S. wrote the manuscript with inputs from R.Y. and Q.S.. All  
349 authors made comments.

# Supplementary Files

This is a list of supplementary files associated with this preprint. Click to download.

- [RIXSdetwinnedFeSeSI.pdf](#)